Results in Engineering 16 (2022) 100700

Contents lists available at ScienceDirect

Results in Engineering

journal homepage: www.sciencedirect.com/journal/results-in-engineering

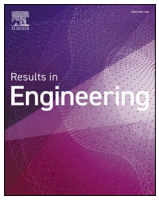

Understanding the local pitting corrosion characteristics of carbon steel in CO_2 corrosion environment using artificially machined pits

Frederick O. Pessu [a,*], Eman Saleem [b], Cayetano Espejo [a], Anne Neville [a]

[a] Institute of Functional Surfaces, School of Mechanical Engineering, University of Leeds, LS2 9JT, UK
[b] Kuwait Oil Company, P.O Box 9758, Ahmadi, Kuwait

ARTICLE INFO

Keywords:
CO_2
$FeCO_3$
Uniform corrosion
Pitting corrosion
Artificial pit
Local pH

ABSTRACT

Carbon steel remains the most commonly used material in CO_2 – containing oilfield, and other energy applications. Pitting corrosion is a prominent form of corrosion attack on carbon steel, and linked to the formation of non – protective iron carbonate ($FeCO_3$) films and/or their breakdown. The conditions for local breakdown of $FeCO_3$, and other fundamental aspects of pitting corrosion are still not clearly understood; particularly in relation to the evolution of the local chemistry within active pits. Local distribution of corrosion activities/species is likely to influence $FeCO_3$ formation; evolution and properties to support and/or impede pit propagation. This study investigates the local corrosion environment within an artificially machined pits to understand the local pitting corrosion behaviour. It focuses on the local evolution of $FeCO_3$ and pitting corrosion. Pits with specific geometry on X65 carbon steel samples are exposed to two different environments: pH of 4 and 5.9 for 168 h. Tests were performed at atmospheric pressure and 60 °C in 1 M NaCl solution. Linear polarization technique was implemented in combination with a suite of post-experiment surface analysis: Scanning Electron Microscopy, X-ray diffraction, 3D-profilometry and Raman spectroscopy for assessing overall corrosion rate, localised corrosion products and pitting characteristics. Results show that at both pH levels, more crystalline $FeCO_3$ was formed within the pits than at the top surfaces. The size and compactness of $FeCO_3$ decrease from the base of the pits towards the top surfaces, which correlates with the extent of pitting corrosion within the pit and the spatial variation in the local chemistry.

1. Introduction

Carbon steel is the most commonly used pipeline material for most CO_2 - containing energy production systems; including oil and gas and geothermal, and carbon capture, utilization and storage (CCUS) systems. This is because of its relatively low cost and metallurgical adaptability. However, such gains are undone by the huge economic and environmental costs caused by corrosion [1–3]. Corrosion in these energy systems is caused by dissolved acid gases in reservoir brines, primarily CO_2 and H_2S gas [2]. Pitting and/or localized corrosion is the most unpredictable form of corrosion attack on carbon steel pipelines deployed in CO_2 - containing environments [4]. Classical pitting corrosion is often associated with passive alloys and occurs when there is a local breakdown of a passive oxide film [5]. A key component in establishing a sustainable galvanic mechanism to drive pitting corrosion is the local chemistry of the pit. For passive alloys such as stainless steels, an active pit will have a lower pH than the surrounding passive interfaces acting as the cathode. Local acidification is driven by an autocatalytic process that supports preferential corrosion of local anodic pits [6,7]. In this case, the galvanic effect between anodic and cathodic areas is often measurable.

Pitting corrosion in carbon steel is believed to occur when there is a poorly formed and/or local removal of iron carbonate ($FeCO_3$) [4,8–10] or iron sulphide (Fe_xS_y) [11] corrosion product layer. When a fully adherent, compact and persistent $FeCO_3$ is formed, uniform corrosion can be supressed to an industrially acceptable safe limit of 0.1 mm/yr [2,12]. This is achieved by $FeCO_3$ establishing a diffusion barrier and blocking electrochemically active sites on the steel surface [13,14]. The occurrence of poorly formed $FeCO_3$ corrosion product layers, and pit initiation and propagation represents an intermediate between the extremes of a completely uniform corrosion attack and fully protective corrosion interface by $FeCO_3$ [8–10]. The evolution of pitting corrosion of carbon steel in CO_2-saturated environments has been reported to be driven by some form of localised galvanic effect between $FeCO_3$ covered

* Corresponding author.
E-mail address: f.o.pessu@leeds.ac.uk (F.O. Pessu).

https://doi.org/10.1016/j.rineng.2022.100700
Received 14 September 2022; Received in revised form 13 October 2022; Accepted 13 October 2022
Available online 18 October 2022

areas acting as cathodes, and exposed areas of carbon steel acting as the anode [4,12,15]. However, with respect to carbon steel, there is a lack of understanding of the local corrosion characteristics within an active pit, especially concerning the question of whether the local acidification model that precedes pit propagation in stainless steels also applies to carbon steel. Pitting corrosion processes have been shown to be influenced to varying degrees by a wide range of parameters to such as temperature, pH and presence of acetic acid and brine chemistry. This is often correlated on the effect of these parameters on the mechanisms and kinetics of $FeCO_3$ and/or Fe_3O_4, depending on the specific environment [3,8–10,16,17]. It is postulated that these parameters could also influence the local chemical speciation and electrochemical properties of an active pit.

In a previous study [16] in CO_2-saturated environments at 80 °C, some active pits on carbon steel self-healed after 168 h and evidence of deposits of $FeCO_3$ was found within the pits. This suggested that the internal cavity of the pits was electrochemically active and dynamic in terms of changes in speciation of ions and surface properties with time. There was also evidence of high pit density on carbon steel surfaces exposed to CO_2 corrosion environments, which appeared underneath a porous and semi-protective $FeCO_3$ film [14,16]. The localised galvanic driving force for pitting corrosion is usually preceded by uniform corrosion [12], which underpins the stochastic distribution of different phases: ferrite - cementite within steel microstructure [3,18].

There have also been several attempts by researchers to investigate the local galvanic mechanism driving pitting corrosion of carbon steel in CO_2 corrosion environments. Han et al. [15], and Zhang and Cheng [4] investigated the galvanic effect using a modified version of the artificial pit by Turnbull et al. [19]. In Han et al.'s [15] design, an anode with an adjustable depth was used as a flush pit and closely surrounded by a cathode area covered with protective $FeCO_3$ which is ~1000 times larger than the anode. It was observed that the galvanic current between the bare steel acting as the anode and $FeCO_3$ covered cathode area decreases with time due to the deposition of $FeCO_3$ at the anode [15] with time. In Zhang and Cheng's [4] design, the anode and cathode areas were physically separated by an epoxy resin and a galvanic current was measured between the $FeCO_3$ covered cylindrical cathode and a bare concentric anodic surface, forming a flush pit. In both studies, there was evidence of galvanic effects between the anodic and cathode surfaces. However, these results did not account for the evolving local galvanic currents between local anodes and cathodes within the anodic surface. Pitting corrosion could also be occurring at the anodic surfaces which is driven by microscopic galvanic mechanisms between local anodic and cathodic areas. Other localised changes in the electrochemical and ionic properties of the corrosion interfaces could also be taking place, especially as the local current at these anodes could be at least twice as much as at the cathodes [15]. While this can often be linked to the distinctive corrosion behaviour of carbon steels, especially in relation to current understanding on the evolution of pitting corrosion [16], there has been little or no studies focused on understanding the evolution of a local pit with time.

This study therefore aims to investigate the local corrosion interfacial properties of an artificially machined pit without a pre-defined anode and cathode areas on carbon steel in CO_2-saturated environments, starting at pHs 4 and 5.9, and temperature of 60 °C in 1 M NaCl. The method explored in this study is the first stage of an experimental strategy to understand the corrosion characteristics of the local cavity of an active pit. This study also aims to assess the preferential distribution of electrochemically active and/or precipitable species that forms $FeCO_3$ within a pit and its surrounding interfaces. In addition, this work seeks to establish an understanding of the chemical speciation profile of an active pit and how it could influence the progression of local electrochemical activities, $FeCO_3$ film formation characteristics, and pit growth.

2. Experimental procedure

Experiments were conducted in a 1 M NaCl solution saturated with CO_2 gas at 60 °C and atmospheric pressure. Pit geometry was also tracked and correlated to the surface properties of the pits. The pHs of the solutions were not controlled but were measured at the start and end of each tests.

Materials: X65 carbon steel specimens were used as the working electrodes in a three-electrode cell in each experiment. Typical X65 carbon steel possesses a ferritic/pearlitic microstructure with nominal composition, as provided in Table 1.

The carbon steel was sectioned into 10 mm × 10 mm x 5 mm specimens with an exposed surface area of 1 cm^2. A single artificial pit of ~200 μm diameter and depth of ~250 μm was created using a drill on the steel surface before specimen preparation. Wires were soldered to the back of each test specimen and then embedded in a non-conducting resin. Aluminium foil was used to cover the top side of the machined pits to prevent resin from entering the pits. Prior to the start of each experiment, test specimens were wet-ground with 1200 silicon carbide grit paper, degreased with acetone, rinsed with distilled water and dried with compressed air before pre-experiment surface characterization using a NPFlex 3D non-contacting profilometer. An example of the characterized pit geometry before a test is shown in Fig. 1. Surface profilometry analysis was also carried out after the test. A total of 5 specimens were used per litre of solution. This experiment was repeated up to three times, while post experiment analysis was also repeated twice.

Brine preparation and test conditions: Two different test solutions containing 1 M NaCl, with different starting pHs, were used in this study. The pH of the test solutions were allowed to evolve throughout the test but measured at the start and end of each experiment. The test solution was saturated with CO_2 for a minimum of 12 h prior to starting each experiment to de-aerate the test environment and completely attain CO_2 saturation in order to simulate oilfield conditions. CO_2 was also bubbled into the system throughout the duration of every experiment at atmospheric pressure and a constant temperature at 60 °C. The measured pHs before (pH measured after saturation with CO_2 at test temperature) and after the test are provided in Table 2.

In-situ electrochemical measurements: Electrochemical measurements were conducted on two specimens per test. Each specimen formed the working electrode in a three-electrode cell set-up which also comprised of an Ag/AgCl reference electrode and a platinum counter electrode. The tests were repeated 3 times to ensure repeatability. Linear Polarization Resistance (LPR) measurements were performed by polarizing the working electrode every 15 min ± 15 mV about the open circuit potential (OCP) at a scan rate of 0.25 mV/s to determine the polarization resistance (R_p). Tafel constants were estimated using Equation (1) [20,21];

$$\beta_a = \frac{2.303RT}{\alpha_a F} \text{ and } \beta_c = \frac{2.303RT}{\alpha_c F} \quad (1)$$

where α_a and α_c are coefficients for anodic and cathodic reactions, corresponding to 1.5 and 0.5 respectively, according to Bockris et al. [22]. Tafel constants; β_a = 43.11 mV/decade and β_c = 132 mV/decade were used in conjunction with R_p and Faraday's Law to determine *in-situ* corrosion rates. This gives a Stern-Geary coefficient of 14.11 mV/decade which was used for both test environments.

Corrosion product characterisation: After each experiment, the test specimens were carefully removed from the solution, gently rinsed with distilled water, dried and stored under vacuum before post-experiment analysis. Corrosion product characterisation was carried out after the shortest possible specimen storage time. SEM analysis was used to identify the corrosion products formed at the base, the internal walls and the top surface of the pit. SEM analysis was conducted twice on two separate samples from 2 repeated experiments. Results from these

Table 1
Elemental composition of X65 (UNS K03014) steel (wt. %).

C	Si	P	S	Mo	Mn	Ni	Nb	V	Fe
0.15	0.22	0.023	0.002	0.17	1.42	0.09	0.05	0.06	97.81

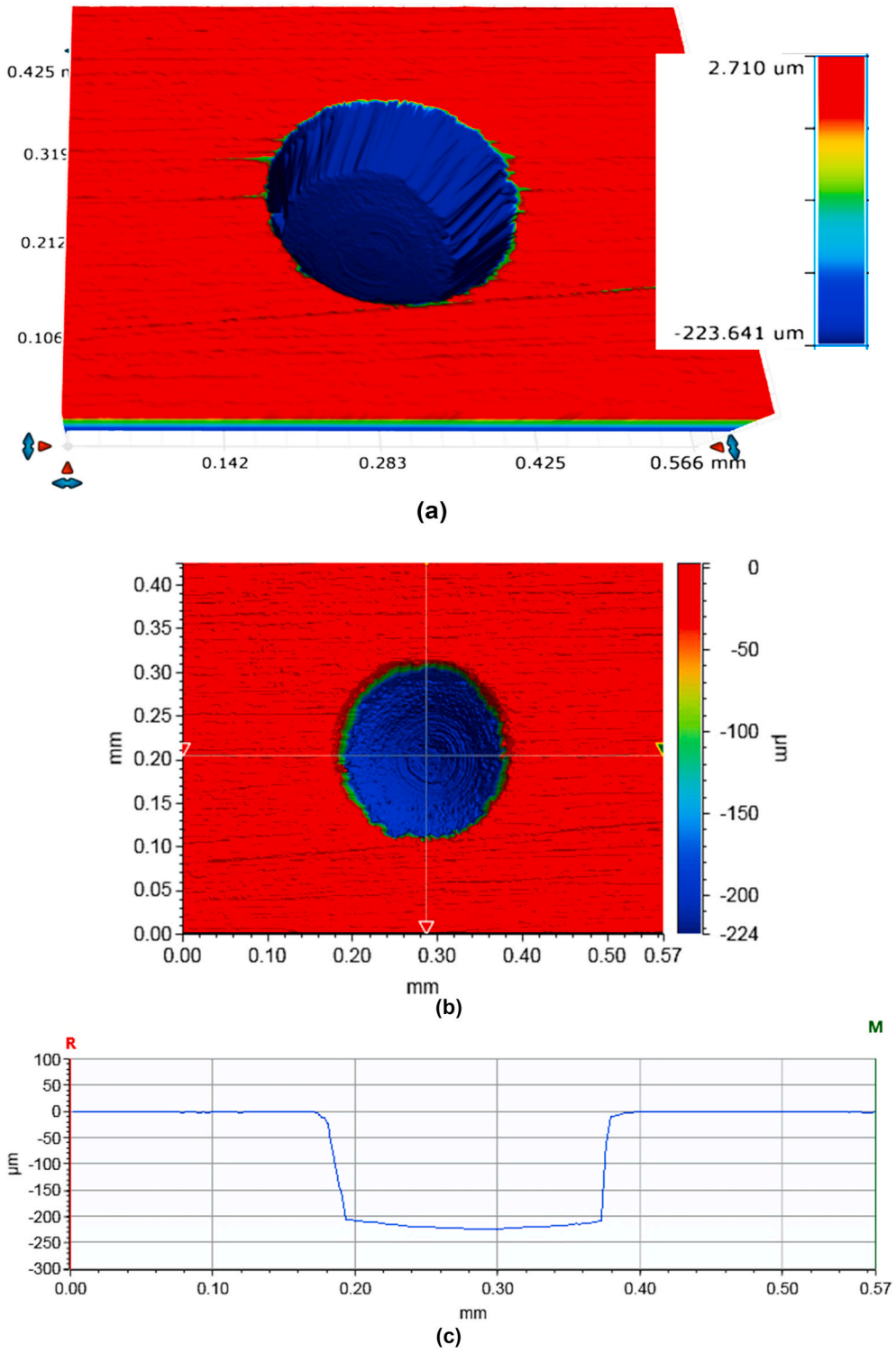

Fig. 1. Surface profilometry analysis of X65 specimen showing the dimensions of an artificially machined pit before immersion into a CO_2 corrosion environment for 168 h; (a) 3D image, (b) 2D top view image and (c) Surface profile showing depth and diameter of the artificial pit.

Table 2
Measured bulk pH before and after experiment.

	Bulk pH measurement at 60 °C			
	Test 1 (Un-buffered)		Test 2 (Buffered with 0.012 M $NaHCO_3$)	
	Start of test	End of test	Start of test	End of test
1st Measurement	4.0	5.8	5.9	6.1
2nd Measurement	4.0	5.8	5.9	6.2

repeated SEM analysis are presented in this paper. XRD patterns were collected from the top surface of the specimens using a Bruker D8 diffractometer. It is equipped with a LynxEye detector, employing Cu Kα radiation with an active area of 1 cm^2 programmable di-vergence slits. Scans were performed over a range 2θ = 10–70° using a step size of 0.033 per second, with a total scan time of approximately 50 min. The results were analysed by comparing with individual crystal standards from available database. Raman analyses were conducted using a Renishaw inVia microscope, using a 488 nm wavelength laser excitation source, edge Rayleigh filter and a 2400 lines/mm grid, delivering the scattered signal to a CCD detector and and providing 1 cm^{-1} spectral resolution. The selected objective lense was a Leica 0.75 NA ×50 magnification, producing a spot size smaller than 1 μm in diameter. Spectra were obtained using 0.5 mW laser power at 1s exposure time, ensuring no damage or thermal effects were induced on the corrosion products. 50 accumulations were obtained to increase the signal to noise ratio. Raman analysis was also deployed to characterize the surface properties of corrosion products formed at the base, internal walls and the top surface of the pit.

Characterization of pitting corrosion damage: Surface profilometry was used in this study to evaluate pitting corrosion attack. This was carried out after removing corrosion products from specimens using Clarke's solution in an ultrasonic cleaning bath. Profilometry was used to track the changes in the geometry of the machined pit with emphasis on the base, internal walls and top of the pits. The NPFlex 3D profilometer was used to identify the discrete geometrical properties of evolving pits within the artificial pit. Carefully chosen thresholds were used to obtain detailed pitting corrosion characteristics of the artificial pit. 3D and 2D images showing the evolution of the artificial pits are also provided as visual evidence of pitting corrosion behaviour.

3. Results and discussion

3.1. Electrochemical characteristics and corrosion product formation

Fig. 2 presents the electrochemical responses of tests in pH 4.0 (unbuffered) and 5.9 (buffered) based on linear polarization resistance measurements and analysis. The general corrosion rates, corrosion potential and average thickness loss are presented in Fig. 2(a), (b) and (c), respectively. The average thickness loss was extrapolated using Faraday's equation for average corrosion rate (mm/yr) for the total duration of the test. It is based on the assumption that electrochemical responses recorded in the LPR measurements was uniformly distributed across the entire exposed surface area (~1 cm^2). Referring to Fig. 2(a), the average corrosion rate of the specimens in pH 4.0 solution is higher than that in pH 5.9 solution. The different stages of the corrosion process show an initial increase in corrosion rate preceding periods of stable and decreasing corrosion rates in both corrosion systems. The decrease in corrosion rate in both systems is driven by establishment of a Fe_3C/$FeCO_3$ corrosion product layer on the steel surface [2,23] as shown by the SEM images in Fig. 3. $FeCO_3$ formation on both samples is confirmed by the XRD patterns shown in Fig. 4. $FeCO_3$ formation correlates with the increase in open circuit potential (OCP) shown in Fig. 2(b). The difference in morphology of $FeCO_3$ formed in tests at pH 4.0 and 5.9 also correlates to the level of film protectiveness depicted by the corrosion rate data in Fig. 2(a). At lower pH, the environment is more aggressive, causing higher Fe^{2+} dissolution, and therefore higher rate of solution saturation and $FeCO_3$ formation. However, the magnitude of corrosion rate is still higher since the morphology of $FeCO_3$ at the top surface is mainly amorphous, porous and semi-protective as shown in Fig. 3 (a). The XRD pattern in Fig. 4 show the absence of a strong peak for $FeCO_3$ at 32 2θ formed at pH 4.0, and only a weak peak at 35.5 2θ. This correlates with the visual evidence of a continuous amorphous $FeCO_3$ corrosion surface layer at the top surface shown in the SEM image in Fig. 5 (b) for pH 4.0. In pH 4.0 test system, there is therefore a clear absence of crystalline $FeCO_3$ at the top surface. In the high pH solution, the morphology of $FeCO_3$ is still mainly amorphous at the top surface, but with a significant amount of $FeCO_3$ crystals as shown in Fig. 3(d). These electrochemical responses translate to an estimated thickness loss of 70 μm and ~33 μm over 168 h for pH 4.0 and pH 5.9 solutions respectively, and shown in Fig. 2(c).

The absence of strong peaks for $FeCO_3$ (at pH 4.0) at 32° 2θ indicates that the $FeCO_3$ formed on the top surface of corroding steel at this pH is non-crystalline (amorphous). The presence of a peak at 32° 2θ on the top surface of the corroding steel at pH 5.9 confirms the presence of a small degree of crystalline $FeCO_3$ [24–26]. At pH 4.0, amorphous and porous $FeCO_3$ is observed to cover the top surface of the steel, while the base of the artificial pits consists of porous and relatively small-sized $FeCO_3$ crystals (Fig. 3 (c)). There is also evidence of an inner corrosion product layer underneath $FeCO_3$ crystals at the base of the pit (See Fig. 3(c)). This inner layer appears to be amorphous $FeCO_3$, similar in nature to the amorphous layer on the top side of the surface shown in Fig. 3(a). This observation is consistent with the findings reported by Guo et al. [27], where it was reported that the increase in nucleation rate of $FeCO_3$ without crystal growth on carbon steel surface with time is linked to low bulk pH. Low pH has been shown[27] to increase nucleation rate than crystal growth once a critical saturation ratio (S_c) is exceeded. This has the tendency to promote the formation of amorphous $FeCO_3$. This has also been confirmed in a separate study [16]. Saturation ratio (S) in this case represents the ratio of concentration of species; [Fe^{++}] and [CO_3^{2-}] for $FeCO_3$ formation to the solubility product of $FeCO_3$ (K_{sp}), and precedes nucleation and crystal growth [2,27]. A saturation ratio of $S \geq 1$ is usually required for nucleation to start. The inner amorphous $FeCO_3$ layer observed at the base of the pit at pH 4.0 in this work is likely to have been formed first before the crystalline $FeCO_3$ is formed as an outer layer. This is due to the initially low bulk pH and the gradual increase in bulk pH as presented in Table 2. It is believed that a similar trend in pH change could also be occurring within the local pit cavity, albeit by a higher magnitude, and driving the transition from an amorphous inner layer to a crystalline outer layer of $FeCO_3$ at the base of the pit [27]. Bulk pH change is related to the buffering effect of the corrosion process. This has already been reported by several authors [12,27].

The SEM images of the specimens from pH 5.9 solution also show similar repeatability. Referring to Fig. 3(d) to (f), the base of the pits are observed to be covered with larger crystals of $FeCO_3$ than at pH 4.0. The crystals also appear to be more compact at the base of the artificial pit, while a combination of a dominant amorphous layer and dispersed amount of smaller sized crystals are observed at the top surface (Fig. 3 (d)). $FeCO_3$ crystals formed at this pH are expected to be providing better protection against uniform corrosion within the artificial pit. This is because the pH is suspected to be higher at the base of the pit than at the top surface of the pit based on the basis of the mechanism explained for solution at pH 4. This is due to a combination of lower critical saturation ratio (S_c) requirement at high pH, and the buffering effect linked to the initial concentration of Fe^{2+} produced at the base of the pit at the start of the corrosion process [2,27]. The relationship between pH at the top surface and base of pit, with $FeCO_3$ formation, crystallization and distribution observed in this study is consistent with findings in literature [12,15,27] (for studies mainly focused on pH in bulk solutions). Low bulk pH causes the formation of amorphous/non-crystalline $FeCO_3$, while bulk pH causes the formation of crystalline $FeCO_3$ [14,16,

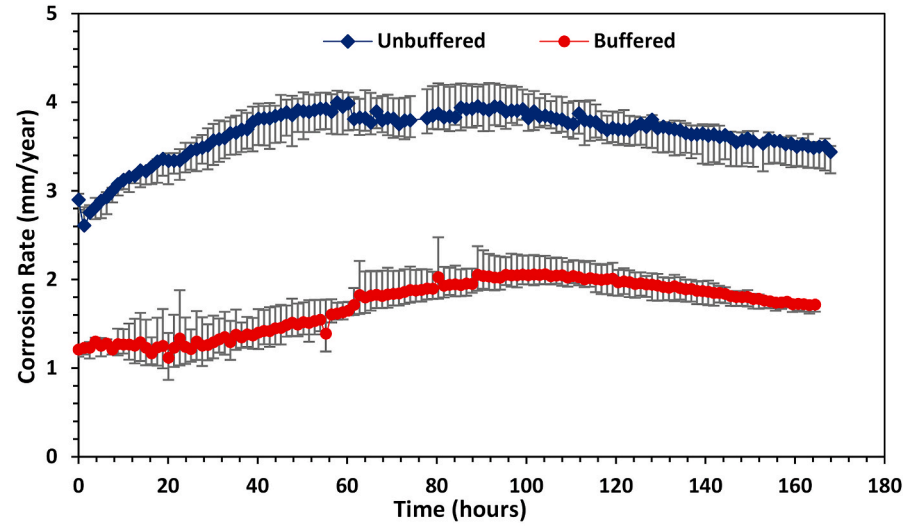

(a)

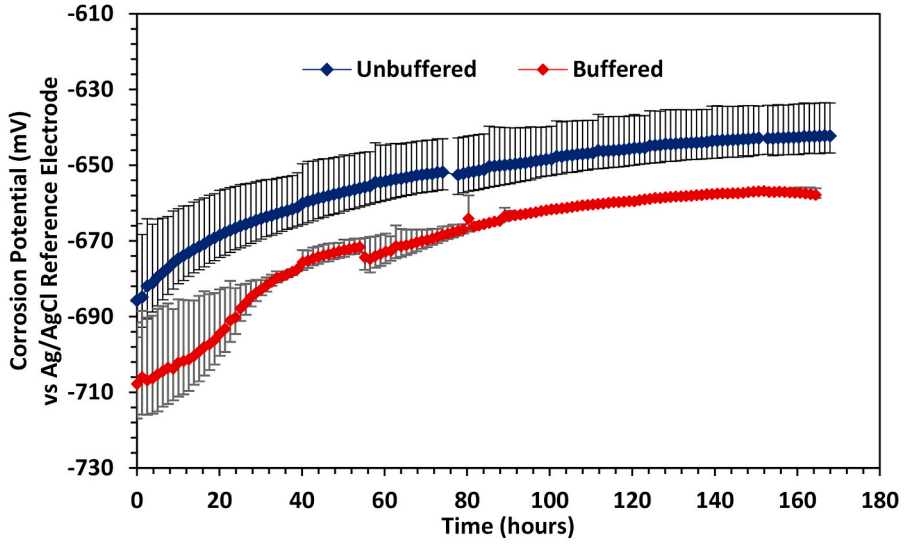

(b)

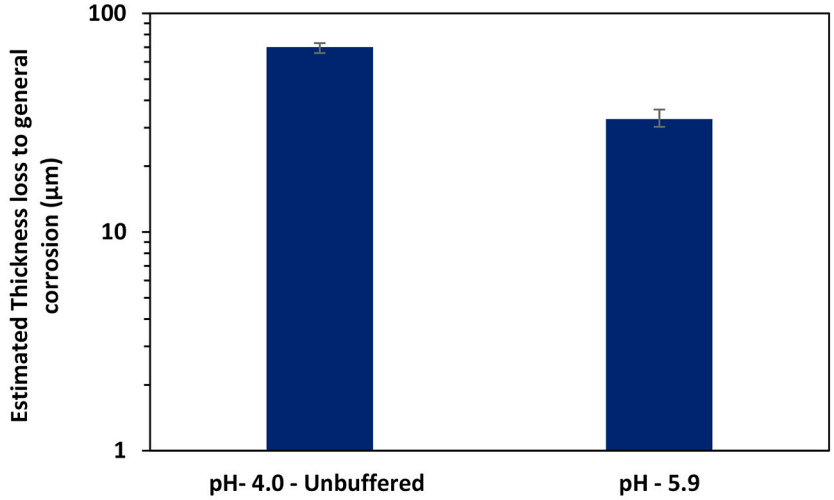

(c)

Fig. 2. Corrosion rate for X65 carbon steel in 1 M NaCl solutions saturated with CO_2 at 60 °C at different pH; 4.0 (un-buffered) and 5.9 (buffered) over 168 h (a) Average corrosion rate (b) Average corrosion potential and (c) Average estimated thickness loss due to general corrosion after 168 h.

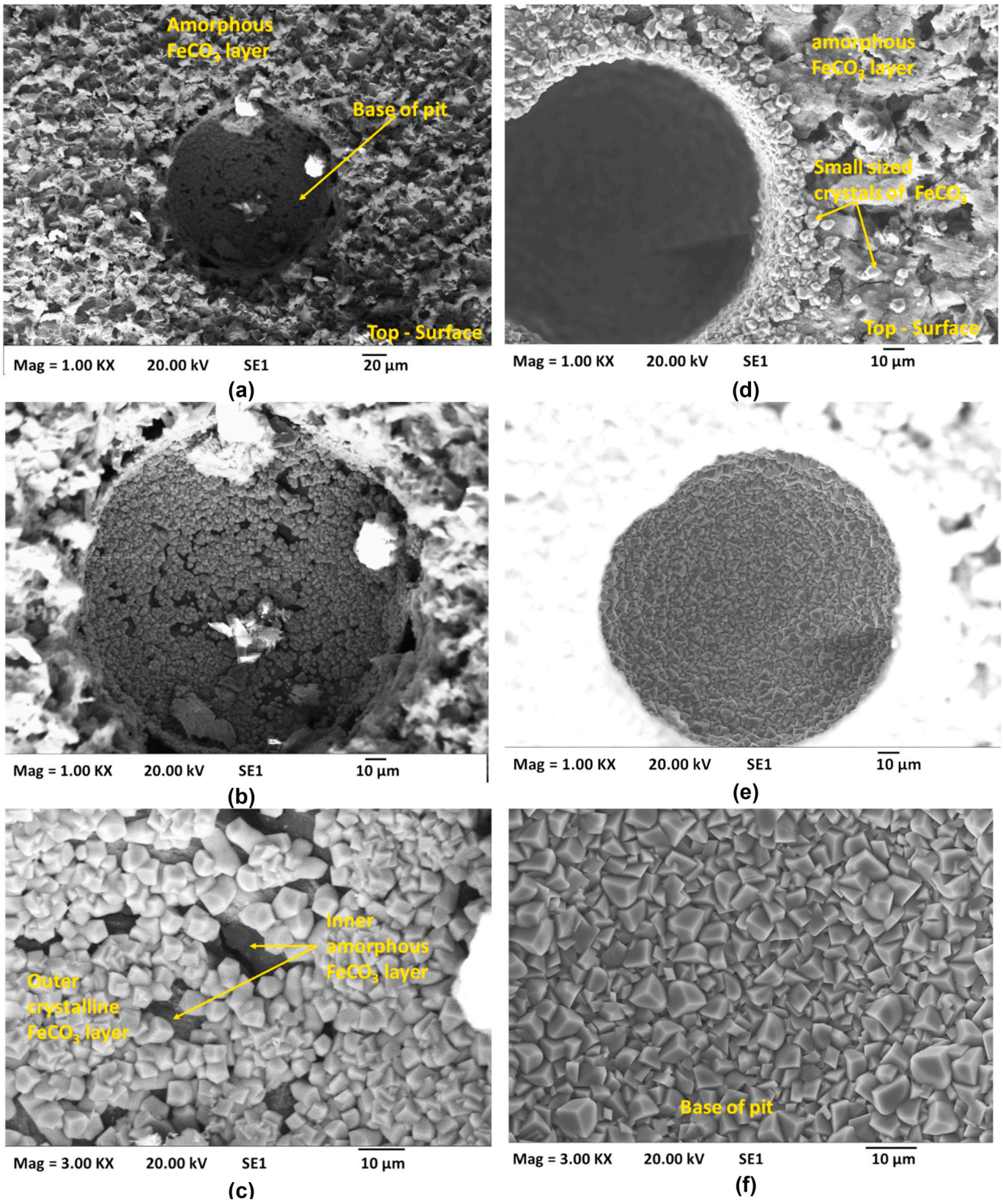

Fig. 3. SEM images for corrosion product formed on X65 carbon steel in 1 M NaCl solutions saturated in CO_2 at 60 °C after 168 h (a) Top surface of sample from test at pH 4.0 (b) Sample from test at pH 4.0 showing the base of the pit (c) $FeCO_3$ at the base of artificial pit in sample from test at pH 4.0, (d) Top surface of sample from test at pH 5.9 (e) Sample from test at pH 5.9 showing the base of the pit, and (f) $FeCO_3$ crystals at the base of artificial pit in sample from test at pH 5.9.

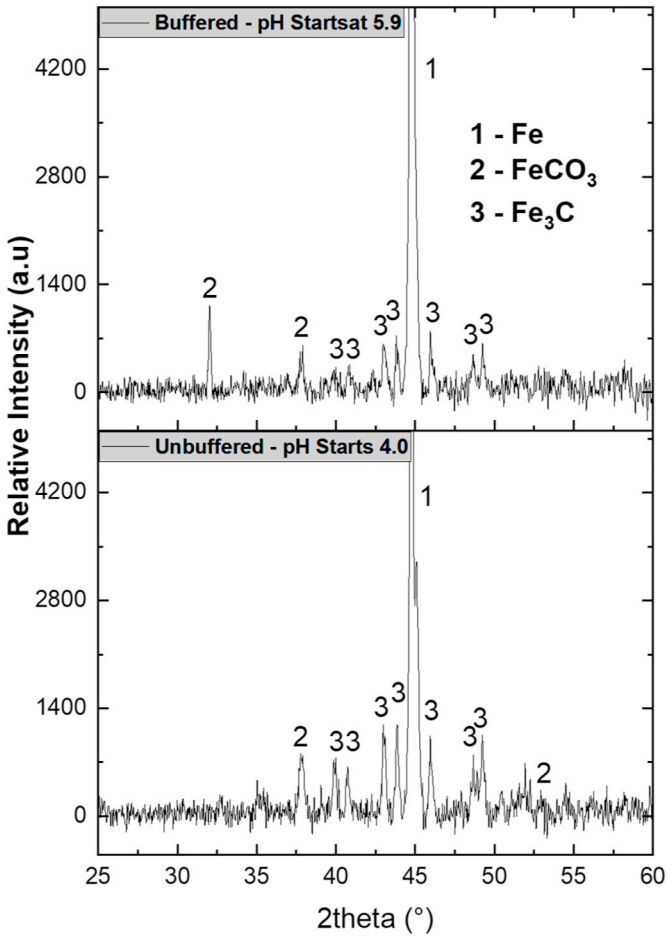

Fig. 4. XRD pattern for corrosion product formed on X65 carbon steel 1 M NaCl solutions saturated with CO_2 at 60 °C and different pH concentrations; 4.0 and 5.9 after 168 h [24–26].

27]. At lower pH the critical saturation ratio (S_c) at which $FeCO_3$ crystal growth occurs increases. Nucleation of $FeCO_3$ starts when saturation is attained, while the rate of nucleation increases rapidly without crystal growth when the critical saturation (S_c) has been exceeded at lower pH, often leading to higher [Fe^{2+}] generation, and the formation of amorphous $FeCO_3$. Dugstad [28] also stated that the rate of nucleation and crystal growth is strongly linked to the relative saturation ratio (σ) (σ = S-1). A lower relative saturation (σ) favours crystal growth and a higher relative saturation (σ) increases nucleation rate. A higher crystal growth rate leads to a more compact and protective $FeCO_3$ [14,29] similar to SEM images shown in Fig. 3(e) and (f) at the base of the pit at pH 5.9. Relative saturation requirement for $FeCO_3$ crystal formation also decreases with increasing pH for a system with the same Fe^{2+} concentration. Thus, an amorphous $FeCO_3$ will form favourably at lower pH due to the restriction of its formation mechanism to nucleation rather than crystal growth [29]. Therefore, the change in crystallinity of $FeCO_3$ from the base of the pit to the top surface strongly suggests the direction of change in the pH from the base of the pit to the top surface.

3.2. Corrosion characteristics within an artificial pit

The SEM images and XRD pattern presented in Figs. 3 and 4 are based on the corrosion process occurring on the overall surface of the samples. The observations described for the top surface above have been shown to differ from the local environment within the artificial pits. SEM images showing $FeCO_3$ formed within the internal pit cavity are provided in Fig. 5 for tests at pH 4.0 and pH 5.9. These images show in detail the nature and morphologies of the corrosion products at the top surface, the internal wall and the base of the pit. The Raman spectra shown in Fig. 6(a) and (b) confirm the morphologies of $FeCO_3$ formed at the top surface, the internal wall and the base of pit for tests at pH 4.0 and 5.9, respectively.

Referring to Fig. 5(a) and (b) for the test in pH 4.0, crystalline $FeCO_3$ was formed at the base of the pit on top of an amorphous layer of $FeCO_3$. This is similar to SEM image described above and shown in Fig. 3 (c). The analysis of the morphology of the $FeCO_3$ within the artificial pit is being used in this paper to infer the local chemical conditions within the pit. Crystalline $FeCO_3$ formed at the base of the pit is clearly semi-protective at pH 4.0 and it is believed to be caused by the gradual increase in local pH and saturation within the pit with time. With influx of H^+ into the pit cavity at the start of test, it is believed that the Fe^{2+} release rate will increase due to the low initial pH. Without an out-flux of H^+, production of Fe^{2+} at anodic sites will cause a buffering effect by driving the reduction of H^+, and H_2 evolution at cathodic sites, increasing local saturation with respect to Fe^{2+} and CO_3^{2-}, causing the local pH to increase, and favour $FeCO_3$ crystal growth at the base of the pit. Similar mechanism has also been reported in Guo et al. [27] for metal – bulk solution interface and supports the sequence of formation of an inner amorphous layer, and followed by an outer crystalline layer of $FeCO_3$ at the base of the pit [29].

For the test at pH 5.9 (Fig. 5(c) and (d)), a similar trend to pH 4.0 is observed. However, the crystals of $FeCO_3$ formed at the base of the pits were found to be more compact and protective. The crystal size was also larger at the base of the pit but becomes smaller sized in the direction from the base through the internal wall, and to the top surface around the artificial pits. This is linked to the increase in local relative saturation (σ) level with respect to $FeCO_3$ formation, with decrease in local interfacial pH in the direction; from the base through the internal wall, to the top surface around the artificial pits. This observation indicates that the local interfacial pH is decreasing, leading to a decrease in $FeCO_3$ crystal growth in the direction from the base of the pit towards the top surface around the pit. This is clearly different from the current understanding of distinct anodic areas in the model of pitting corrosion in stainless steels. The distribution of $FeCO_3$ crystals of different sizes and morphologies (shown in Fig. 5) is linked to the relationship between relative saturation and its effect on nucleation and crystallization of $FeCO_3$ at different locations within the pit; either anodic or cathodic [16,27].

The Raman spectra in Fig. 6 have been analysed and referenced to Langille and O'shea [30]. Referring to Fig. 6 (a) and (b), the Raman spectra of the top surface in both pH environments showed no evidence of strong peaks for $FeCO_3$ indicating mainly an amorphous layer of $FeCO_3$. In Fig. 6(a), it is clear that no Raman sensitive layer is present at the top. At the edge/wall, there are peaks corresponding to hematite/alpha-hydroxides (peaks at 215, 279 and 388 cm^{-1}) [31,32] in combination with amorphous $FeCO_3$ as shown by SEM images in Fig. 5 (a) and (b). Hematite/alpha-hydroxides could be due to the effect of Raman Laser beam or ex-situ contamination. At the bottom of the pit, a clear formation of $FeCO_3$ is confirmed (peaks at 183 and 281 cm^{-1} assigned to T and L lattice modes respectively, 720 cm^{-1} for the in-plane $\nu 4$ CO_3 symmetric deformation and 1085 cm^{-1} corresponding to $\nu 1$ CO_3 symmetric stretching [33]. In Fig. 6(b), at higher pH, the top surface is also a non-Raman sensitive layer. The $\nu 1$ CO_3 peak is also present in the edge/wall, but no $\nu 4$ peak is present, which indicates that the $FeCO_3$ formed here is poorly crystalline. At the base of the pit, the same crystalline $FeCO_3$ spectrum that was found previously in the base of the pit formed at pH 4.0 is observed. The observations from Raman analysis are consistent with the SEM images in Fig. 3(a) and (b) for pH 4.0 and Fig. 3 (d) and (f) for pH 5.9. This confirms the absence of crystalline $FeCO_3$ on the top surface of sample in the pH 4.0 environment and the presence of poorly crystalline $FeCO_3$ at the edge/wall of the pit in sample in the pH 5.9 environment. At the base of the pits, evidence of strong peaks at 1080 cm^{-1} in Raman spectra for both pH 4.0 and pH 5.9 is shown. The intensity of Raman peak for $FeCO_3$ in pH 5.9 was higher than in pH 4.0,

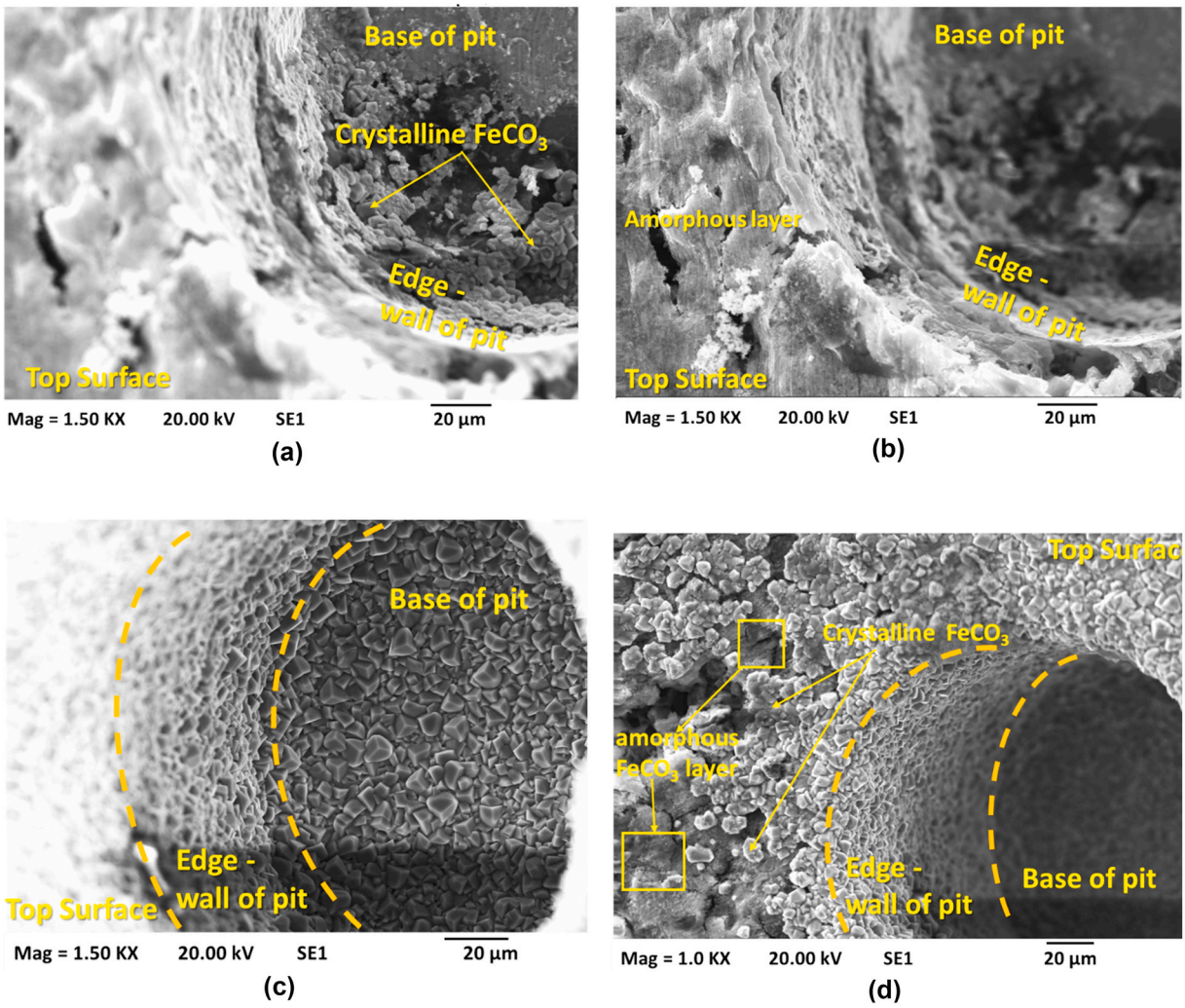

Fig. 5. SEM images of $FeCO_3$ formed inside an artificial pit on carbon steel in 1 M NaCl solution saturated with CO_2 at 60 °C, after 168 h (a) pH 4.0, (b) pH 4.0, (c) pH 5.9 and (d) pH 5.9.

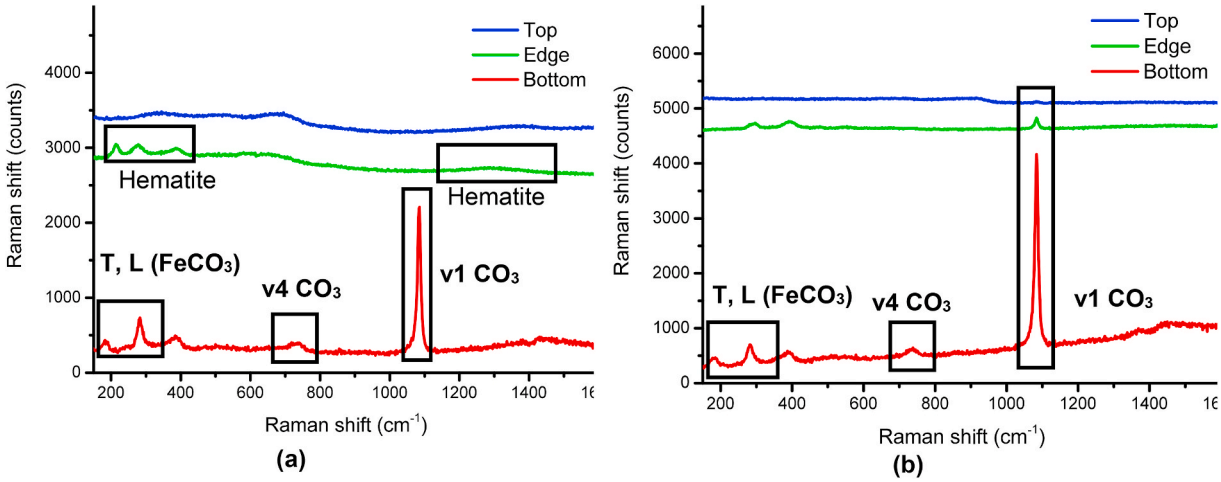

Fig. 6. Raman spectra for corrosion product formed on X65 carbon steel in 1 M NaCl solutions saturated with CO_2 at 60 °C, after 168 h: (a) pH 4.0 and (b) pH 5.9.

which relates to the difference in size and nature of crystals shown in Figs. 3 and 5 for both test environments. It is clear that the local chemistry within the artificial pit is different for both test environments, but changing in a similar direction in terms of decreasing pH from the base of the pits towards the top surface surrounding the pits. It is believed that the distribution of the different nature, morphologies and protective properties of $FeCO_3$ formed within the pits is linked to the distribution of pH and hence $[H^+]$, $[CO_3^{2-}]$ and other precipitable

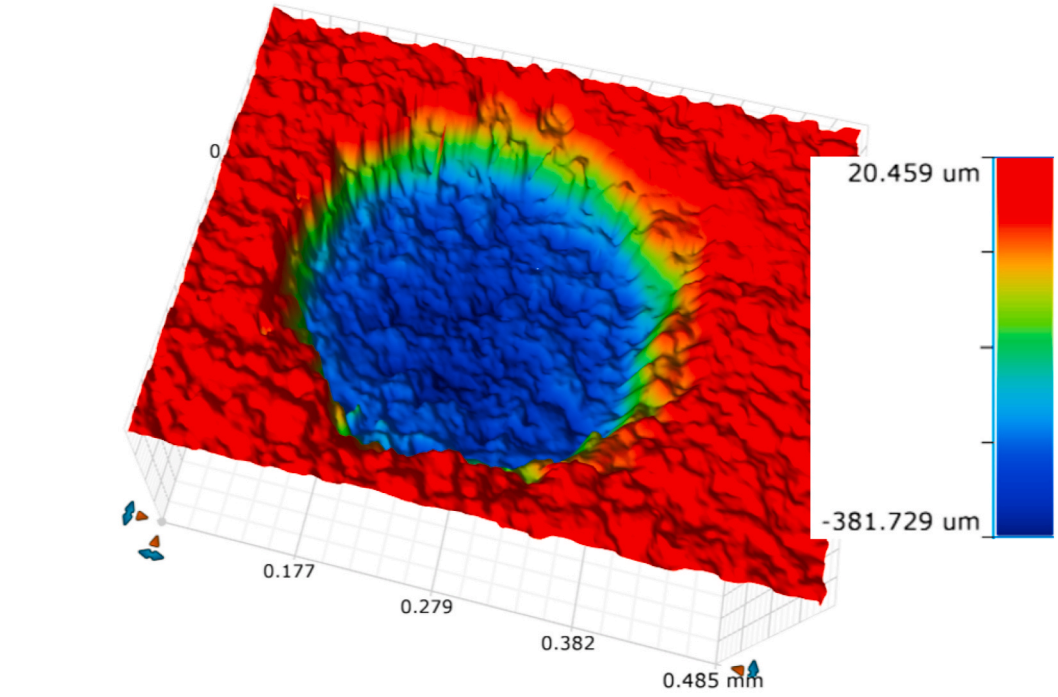

(a)

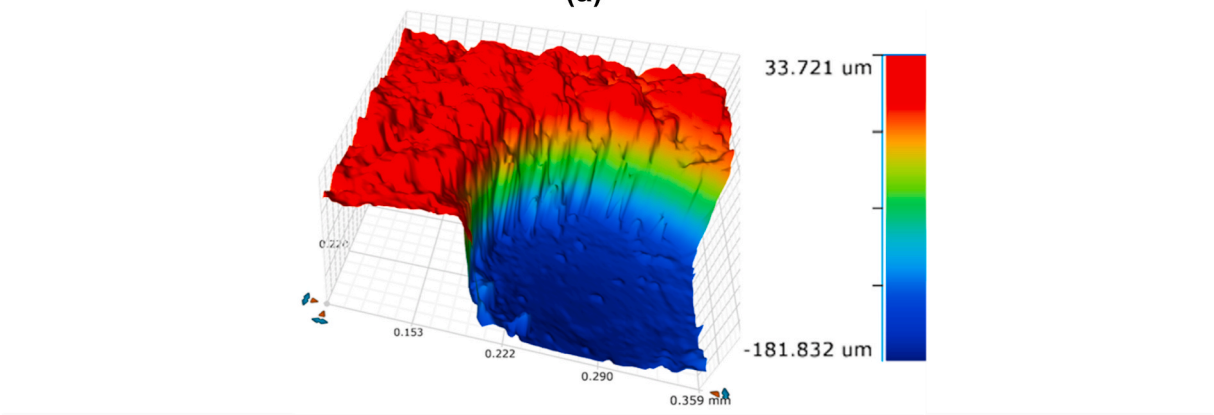

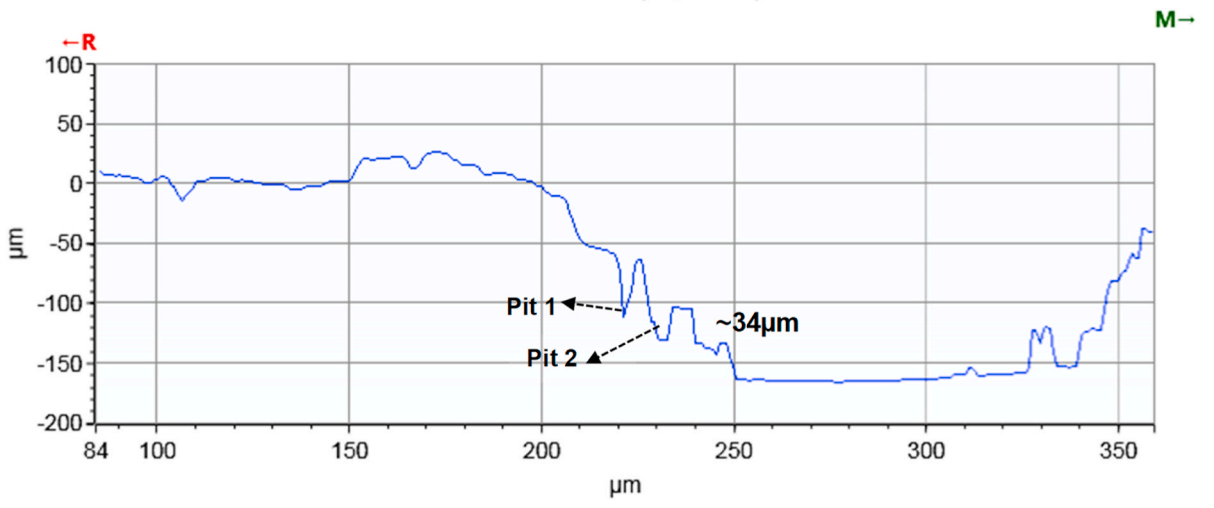

(b)

Fig. 7. Surface profile of artificially machined pits on carbon steel in 1 M NaCl solutions saturated with CO_2 at 60 °C and 4.0 pH after 168 h (a) 3D image of artificial pit (b) 3D and 2D surface profile of base and internal walls of the artificial pit (c) Results from multiple-regional analyses showing identified pits on top surface (d) Results from multiple - regional analyses showing identified pits growing at the base of the pits, and (e) 2D-Surface profile of the base of the artificial pit.

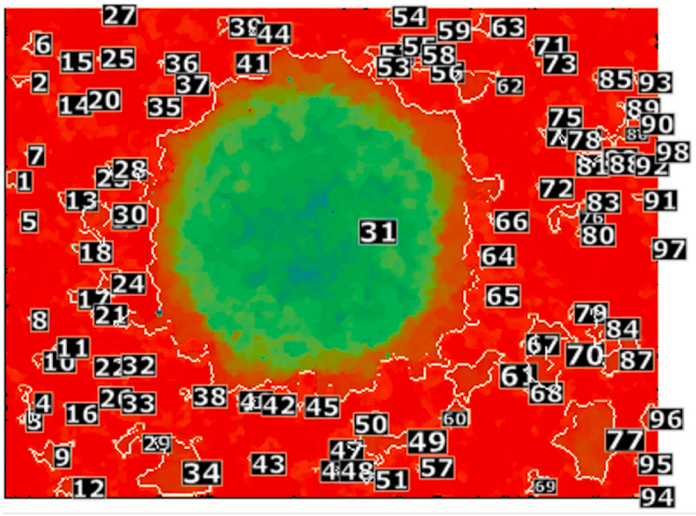

(c)

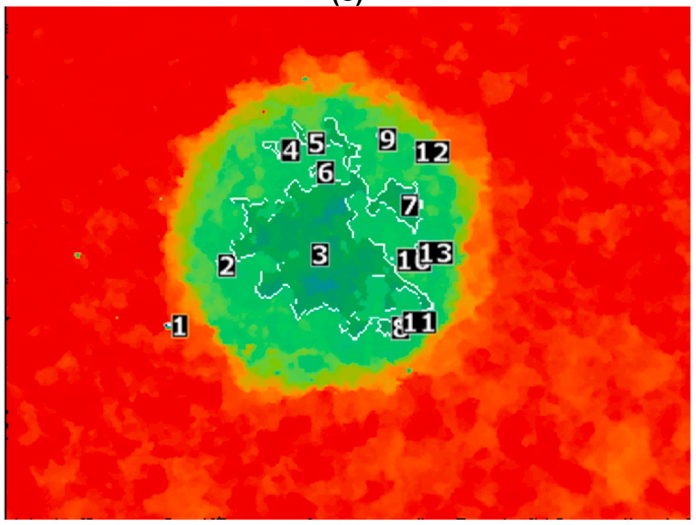

(d)

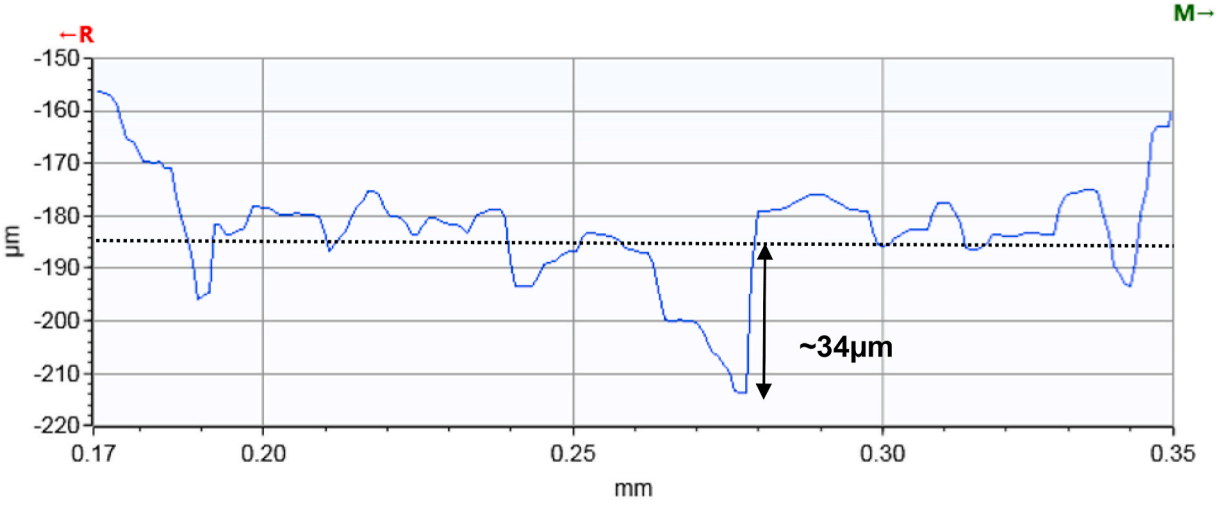

(e)

Fig. 7. (*continued*).

species within the pit. Consequently, this local chemistry is expected to influence the pitting corrosion behaviour in the pits such that parameters such as temperature, mass-transfer etc. that can influence the local distribution of these species within a pit can also influence the rate of growth or healing of pits in carbon steel.

3.3. Pitting corrosion behaviour of artificial pits

Pitting corrosion analysis after removal of corrosion products is presented in Figs. 7 and 8 for tests in pH 4.0 and 5.9, respectively. A sample from each of the repeatable tests at both pH 4.0 and 5.9 solutions was analysed. For the sample from the pH 4.0 solution, results from surface analysis indicate that distinct $FeCO_3$ formation mechanisms were occurring at the top surface, the internal walls and the base of pit. The level of material degradation across all three corrosion interfaces is shown in Fig. 7. Fig. 7(a) and (b) indicates the existence of multiple anodic and cathodic areas at the base of pit and top surface. This is more evident from the identified pits (labelled by numbers) from the results from multiple-region analysis shown in Fig. 7(c) and (d) for the top surface and base of pit respectively, and indicating areas that had preferentially corroded as local anodes. Fig. 7(b) presents the profile of the internal wall of the artificial pit and shows evidence of pitting

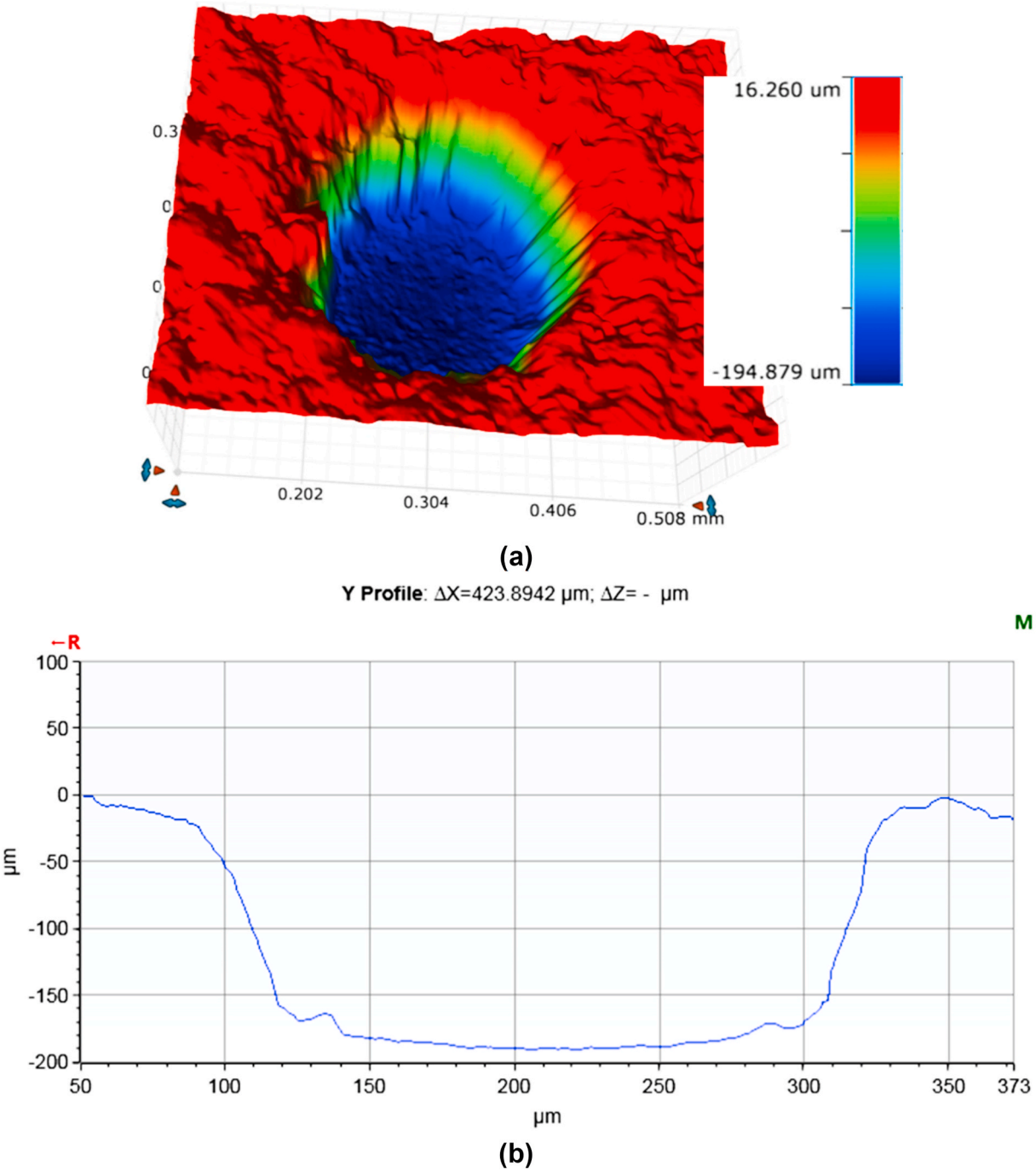

Fig. 8. Surface profile of artificially machined pits on carbon steel in 1 M NaCl solutions saturated with CO_2 at 60 °C and 5.9 pH after 168 h (a) 3D image of artificial pit (b) 2D surface profile of base, internal walls and top surface around the artificial pit (c) Results from multiple-regional analyses showing identified pits on top surface (d) Results from multiple - regional analyses showing identified pits growing at the base of the pit.

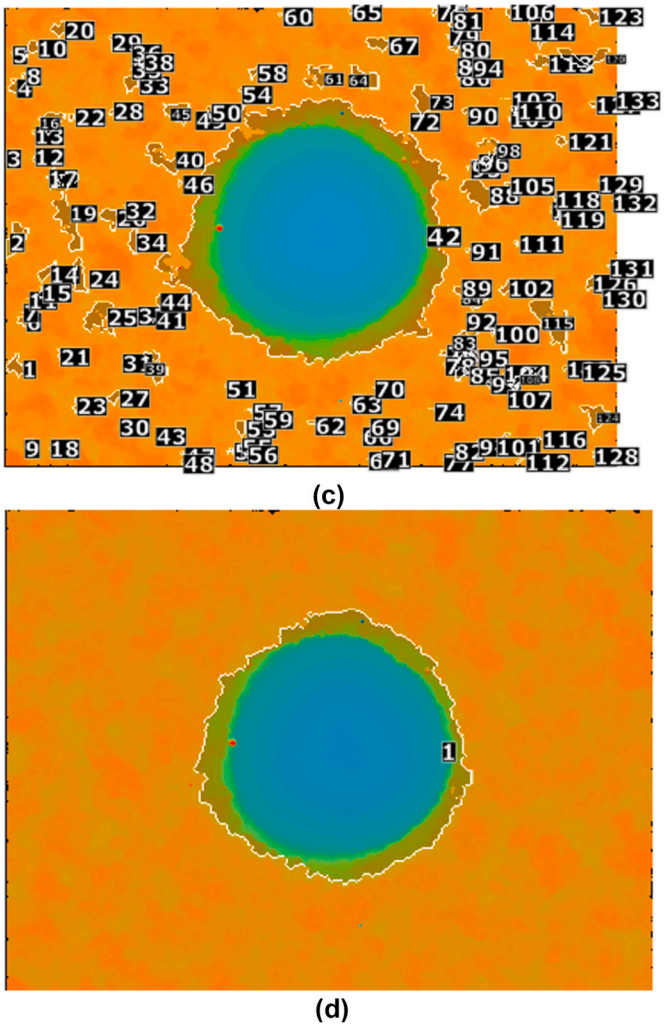

Fig. 8. (*continued*).

corrosion along the walls of the artificial pits just as the morphologies and protective nature of $FeCO_3$ corrosion product is changing along the wall profile of the pit. The profile presented in Fig. 7(b) and (c) shows pitting corrosion occurring along the internal walls and top surface of steel. Pits formed on the top surface are driven by the non-protective and porous nature of amorphous $FeCO_3$ formed as shown in the SEM images in Fig. 3. This is consistent with the literature [15,16], and capable of inducing local galvanic mechanisms, supporting pit propagation to some degree. Pitting corrosion occurring within the pit as observed in this study could be limited by the rate of consumption and distribution of H^+ ions. The rate of local consumption and distribution of H^+ is strongly linked to the evolution of local chemistry and pH, especially within the internal cavity of pit. It is believed that this is also influencing the distribution, morphology and protective capacity of $FeCO_3$ deposited across the corrosion interfaces within the pit. This also determines the distribution of anodic and cathodic regions to drive pit propagation. Therefore, any mass flux or parameters such as velocity that affect the rate of evolution of the concentration profile of H^+ ions inside the pit will influence the propagation of pits.

It is believed that the local pH at the base of the pit started at relatively low pH, the same as the bulk pH. This drives the formation of amorphous/porous $FeCO_3$. As the pH increases due to increase in H^+ reduction/H_2 evolution from corrosion reactions at cathodic and anodic sites, crystalline $FeCO_3$ is formed on top of the amorphous layer. However, in scenario where Fe^{2+} is constantly consumed by, for example, Cl^- to form $FeCl_2$ (as with passive alloys) or other anions migrating into the pits (with constant transfer of products out of the pits), the pH within the pit could potentially remain low enough for $FeCO_3$ to remain unprotective and promote continuous pit growth. It is still unclear what mechanism could potentially help to maintain the local environments within the pit to ensure continuous pit growth. In any case, it is worth noting from this study that an increase in local pH within the pit cavity occurs with time. This is depicted by the higher levels of crystallinity and compactness of $FeCO_3$ at the base of the pit than at the internal wall and top surface. This is shown by the SEM images in Fig. 3 (a)–(c) at pH 4.0, and Fig. 3(d)–(f) at pH 5.9. Despite this fact, the $FeCO_3$ formed at low pH (pH 4.0) appears to be porous and semi-protective with potential for multiple anodic and cathodic sites for the establishment of local corrosion cells as precursor for pitting corrosion within the pit (See Fig. 7(b)–(e)). Pitting corrosion occurring at the base of the pit (initially at a low pH) as shown in Fig. 7(d) and (e) is initiated as a result of the formation of an inner amorphous layer similar to that formed at the top surface. Despite the evidence of continuous increase in local pH over 168 h, the protectiveness of the $FeCO_3$ formed was still not effective in mitigating pitting corrosion.

For samples tested at pH 5.9, a similar trend of corrosion activities occurred at the surface, wall and base of pit. Fig. 8(a)–(b) presents the profilometry analysis showing the level of material degradation across these interfaces. In contrast to the pH 4.0 environment, the corrosion on the surface, internal walls and base of pit appears less aggressive. This correlates with the type of $FeCO_3$ that was observed in Figs. 3 and 5. $FeCO_3$ is more crystalline, compact and protective enough at the base of

the pit to mitigate the occurrence of pitting corrosion. The top surface surrounding the artificial pits shown in Fig. 8(a) and (c) still indicates the occurrence of pitting corrosion at the top surface while $FeCO_3$ layer is still dominated by amorphous $FeCO_3$. The profile of the artificial pit in Fig. 8(c) shows that the walls and base of the artificial pit is less affected by pitting corrosion. This is confirmed by the results of multiple regional analysis in Fig. 8(c) and (d). The pits formed at the top surface is related to the nature of $FeCO_3$ formed and observed in Fig. 5(c) and (d) and Raman spectra in Fig. 6(b). The absence of pits at the base of the pit is because of the effective protection of the compact and crystalline $FeCO_3$ film formed. This is also the case on the sidewalls of the artificial pits as observed by SEM in Fig. 3 (d)–(f) and Fig. 5(c) and (d). This is shown by the pit profile and image in Fig. 8(b).

4. Conclusions

The evolution of the local conditions of artificially machined pits on carbon steel samples have been successfully investigated in reference to the $FeCO_3$ formation and evolution, and the resulting pitting corrosion characteristics for different pHs in CO_2-cantaining environments. The key findings have been summarized as following:

- The local electrochemical activities taking place within the pit have been shown to be different from those taking place at the top surface of the pits. At both locations, the corrosion behaviour is driven by variations in local anodic and cathodic electrochemical activities. This causes a substantial variation in local pH which can be directly correlated to changes in the morphology of $FeCO_3$ formed, its distribution along the pit interfaces, and overall pitting corrosion characteristics of the artificially machined pits.
- At low pH (pH 4.0), non-protective amorphous $FeCO_3$ was the dominant morphology of the corrosion product formed on the surface of the sample, and along the walls of the artificial pit. The crystals of $FeCO_3$ started appearing at the base of the pit on top of an inner amorphous corrosion product layer. At pH 5.9, protective and densely packed crystals of $FeCO_3$ covered the base of the artificial pit. The crystallinity, size of crystals and protectiveness of $FeCO_3$ decreases along the internal walls of the pit towards the "mouth" of the pit. Small sized crystals of $FeCO_3$ were formed as an outer layer at the top surface (around the mouth) of the pit with non-uniform coverage.
- There was more pitting corrosion attack at the top surface area around the artificial pit, the internal side walls, and the base on the artificial pit in the low pH environment (at pH 4.0) than in the buffered environment (at pH 5.9). This is caused by the difference in the speciation of electrochemically active species across the active corrosion interfaces and its influences on the local kinetics of $FeCO_3$ formation. This is evident by the size of pits, pit density and the shape of pits, and the occurrence of pitting corrosion within the artificial pits themselves.

Credit authors statement

Frederick Pessu: Conceptualization, Methodology, Investigation, Formal analysis, & Supervision, Resources, Writing – original draft. **Eman Saleem**: Methodology, Formal analysis and Investigation. **Cayetano Espejo**: Investigation, Formal analysis, Review & editing. **Anne Neville**: Writing - review and supervision.

Declaration of competing interest

The authors declare that they have no known competing financial interests or personal relationships that could have appeared to influence the work reported in this paper.

Data availability

Data will be made available on request.

Acknowledgments

The authors would like to acknowledge Dr Wassim Taleb (Institute of Functional Surfaces, School of Mechanical Engineering, University of Leeds) for his valuable contribution to the collation of XRD data presented in this paper.

References

[1] M.B. Kermani, D. Harrop, The impact of corrosion on oil and gas industry, SPE Prod. Oper. 11 (3) (1996) 186–190.
[2] B.M. Kermani, A. Morshed, Carbon dioxide corrosion in oil and gas production: a compendium, Corrosion 59 (2003) 659–683, 08.
[3] L.D. Paolinelli, T. Pérez, S.N. Simison, The effect of pre-corrosion and steel microstructure on inhibitor performance in CO2 corrosion, Corrosion Sci. 50 (9) (2008) 2456–2464.
[4] G.A. Zhang, Y.F. Cheng, Localized corrosion of carbon steel in a CO2-saturated oilfield formation water, Electrochim. Acta 56 (3) (2011) 1676–1685.
[5] D.W. Hoeppner, Pitting Corrosion: Morphology and Characterization, 1985.
[6] A.S.M. International, Metals Handbook, ninth ed., ume 13-Corrosion, ASM International Ohio, 1987 *(ASM Handbook)*.
[7] M. Schütze, R.W. Cahn, E.J. Kramer, Corrosion and Environmental Degradation: A Comprehensive Treatment, Wiley-VCH, 2000.
[8] S. Papavinasam, A. Doiron, R.W. Revie, Model to predict internal pitting corrosion of oil and gas pipelines, Corrosion 66 (3) (2010) 11.
[9] F. Pessu, R. Barker, A. Neville, CO2 corrosion of carbon steel: the synergy of chloride ion concentration and temperature on metal penetration, Corrosion 76 (2020) 11.
[10] S. Zhang, L. Hou, H. Du, H. Wei, B. Liu, Y. Wei, Synergistic contribution of chloride and bicarbonate ions to pitting corrosion behavior of carbon steel, Corrosion 75 (9) (2019) 1034–1043.
[11] F. Pessu, R. Barker, F. Chang, T. Chen, A. Neville, Iron sulphide formation and interaction with corrosion inhibitor in H2S-containing environments, J. Petrol. Sci. Eng. (2021), 109152.
[12] J.L. Crolet, N. Thevenot, S. Nesic, Role of conductive corrosion products in the protectiveness of corrosion layers, Corrosion 54 (3) (1998) 194–203.
[13] S. Nešić, Key issues related to modelling of internal corrosion of oil and gas pipelines – a review, Corrosion Sci. 49 (12) (2007) 4308–4338.
[14] F. Pessu, R. Barker, A. Neville, The influence of pH on localized corrosion behavior of X65 carbon steel in CO2-saturated brines, Corrosion 71 (12) (2015) 1452–1466.
[15] J. Han, B.N. Brown, S. Nešić, Investigation of the galvanic mechanism for localized carbon dioxide corrosion propagation using the artificial pit technique, Corrosion 66 (9) (2010) 12.
[16] F. Pessu, R. Barker, A. Neville, Understanding pitting corrosion behavior of X65 carbon steel in CO2-saturated environments: the temperature effect, Corrosion 72 (1) (2015) 78–94.
[17] M.C. Folena, R. Barker, F. Pessu, J.A.d.C. Ponciano, A. Neville, CO2 top-of-line-corrosion; assessing the role of acetic acid on general and pitting corrosion, Corrosion 77 (3) (2020) 298–312.
[18] D.A. López, T. Pérez, S.N. Simison, The influence of microstructure and chemical composition of carbon and low alloy steels in CO2 corrosion. A state-of-the-art appraisal, Mater. Des. 24 (8) (2003) 561–575.
[19] A. Turnbull, D. Coleman, A.J. Griffiths, P.E. Francis, L. Orkney, Effectiveness of corrosion inhibitors in retarding the rate of propagation of localized corrosion, Corrosion 59 (3) (2003) 250–257.
[20] S. Nesic, J. Postlethwaite, S. Olsen, An electrochemical model for prediction of corrosion of mild steel in aqueous carbon dioxide solutions, Corrosion 52 (1996) 280–294, 04.
[21] R. Baboian, Corrosion Tests and Standards: Application and Interpretation, Astm International, 2005, pp. 107–117.
[22] J.O.M. Bockris, D. Drazic, A.R. Despic, The electrode kinetics of the deposition and dissolution of iron, Electrochim. Acta 4 (2–4) (1961) 325–361.
[23] F. Farelas, M. Galicia, B. Brown, S. Nesic, H. Castaneda, Evolution of dissolution processes at the interface of carbon steel corroding in a CO2 environment studied by EIS, Corrosion Sci. 52 (2) (2010) 509–517.
[24] I.G. Wood, L. Vocadlo, K.S. Knight, D.P. Dobson, W.G. Marshall, G.D.B. Price, Thermal expansion and crystal structure of cementite, Fe3C, between 4 and 600 K determined by time-of-flight neutron powder diffraction Note:T=540 K, J. Appl. Crystallogr. 37 (2004) 9.
[25] B. Lavina, P. Dera, R.T. Downs, W. Yang, S. Sinogeikin, Y. Meng, G. Shen, D. Schiferl, Structure of siderite FeCO3 to 56 GPa and hysteresis of its spin-pairing transition, Phys. Rev. B 82 (6) (2010), 064110.
[26] O. Sel, A.V. Radha, K. Dideriksen, A. Navrotsky, Amorphous iron (II) carbonate; Crystallization energetics and comparison to other carbonate minerals related to CO2 sequestration, Geochem. Cosmochim. Acta 87 (2012) 61–68, 0.
[27] S. Guo, L. Xu, L. Zhang, W. Chang, M. Lu, Corrosion of alloy steels containing 2% chromium in CO2 environments, Corrosion Sci. 63 (2012) 246–258.

[28] A. Dugstad, Mechanism of protective film formation during CO2 corrosion of carbon steel, in: CORROSION 98, NACE International, San Diego, California, 1998.
[29] M. Gao, X. Pang, K. Gao, The growth mechanism of CO2 corrosion product films, Corrosion Sci. 53 (2) (2011) 557–568.
[30] D.B. Langille, D.C. O'Shea, Raman spectroscopy studies of anti-ferromagnetic FeCO3 and related carbonates, J. Phys. Chem. Solid. 38 (10) (1977) 1161–1171.
[31] D.L.A. de Faria, S. Venâncio Silva, M.T. de Oliveira, Raman microspectroscopy of some iron oxides and oxyhydroxides, J. Raman Spectrosc. 28 (11) (1997) 873–878.
[32] S.J. Oh, D.C. Cook, H.E. Townsend, Characterization of iron oxides commonly formed as corrosion products on steel, Hyperfine Interact. 112 (1–4) (1998) 59–66.
[33] A. Spivak, N. Solopova, V. Cerantola, E. Bykova, E. Zakharchenko, L. Dubrovinsky, Y. Litvin, Raman study of MgCO3–FeCO3 carbonate solid solution at high pressures up to 55 GPa, Phys. Chem. Miner. 41 (8) (2014) 633–638.